DoD HPC UGC Meeting, Seattle 2008 — Clearance No. RVB08.006-487–ESC 08-0867 — Version 0.72

MHD turbulence studies using lattice Boltzmann methods–physical simulations using 9000 cores on the Air Force Research Laboratory HAWK supercomputer

G. Vahala[1], J. Yepez[2], M. Soe[3], L. Vahala[4], J. Carter[5] and S. Ziegeler[6]
[1] *Department of Physics, William & Mary, Williamsburg, VA 23185*
[2] *Air Force Research Laboratory, Hanscom AFB, MA 01731*
[3] *Department of Mathematics and Physics, Rogers State University, Claremore, OK 74017.*
[4] *Department of Electrical & Computer Engineering, Old Dominion University, Norfolk, VA 23529*
[5] *NERSC Division, Lawrence Berkeley National Laboratory, Berkeley, CA 94720*
[6] *High Performance Computing Modernization Program, Mississippi State University, MS 39762*

Most non-spectral CFD algorithms do not scale to many thousands of cores. Here we examine a particular mesoscopic representation of free decaying MHD turbulence that is amenable to massive parallelization to the full 9000 cores available on AFRL SGI Altix 4700 (Hawk). Moreover, our mesoscopic lattice Boltzmann (LB) algorithm will automatically enforce the important $\nabla \cdot \mathbf{B} = \mathbf{0}$ constraint without any need for magnetic field divergence cleaning. Isosurfaces of vorticity and current for LB simulations on a spatial grid of 1800^3 show the long time existence of large scale magnetic and velocity structures. This is in stark contrast to the long time behavior of the velocity isosurfaces which all disintegrate into small scale structures.

Keywords: turbulence, magnetohydrodynamics, lattice Boltzmann equation

I. INTRODUCTION

The effect of magnetic disturbance from solar activities can have devastating effects on earth-based electronics and satellites. In its own right, magnetic turbulence is critical to understand. Here we propose to investigate a mesoscopic representation of the resistive magnetohydrodynamics (MHD) equations

$$\frac{\partial (\rho u_i)}{\partial t} + \frac{\partial}{\partial x_j}\left[\rho u_i u_j - B_i B_j + \left(p + \frac{\mathbf{B}^2}{2}\right)\delta_{ij}\right] = \nu \nabla^2 u_i \tag{1a}$$

$$\frac{\partial B_i}{\partial t} + \frac{\partial}{\partial x_j}\left[u_i B_j - u_j B_i\right] = \eta \nabla^2 B_i, \tag{1b}$$

where ρ is the density, $\mathbf{u}$ the fluid velocity, $\mathbf{B}$ the magnetic field, ν the viscosity and η the resistivity. It is convenient to employ the summation convention over repeated subscripts. The MHD equations are closed by the equation of continuity, divergence-free magnetic field, and an isothermal equation of state:

$$\frac{\partial \rho}{\partial t} + \nabla \cdot (\rho \mathbf{u}) = 0 \qquad \nabla \cdot B = 0 \qquad p = c_s^2 \rho, \tag{2}$$

where the sound speed is set by the number of spatial dimensions $c_s = \frac{1}{\sqrt{3}}$. Unlike standard non-spectral computational fluid dynamic (CFD) algorithms, the mesoscopic lattice Boltzmann (LB) algorithm [1] is not only amenable to massive parallelization but will enforce the $\nabla \cdot \mathbf{B} = \mathbf{0}$ condition to machine accuracy automatically [2].

Normally, the projection from the standard macroscopic ($\mathbf{x}$,t)-space into the higher dimensional ($\mathbf{x}$,ξ,t)-space would not only lead to severe simulation restrictions on the size of the spatial grids due to memory core constraints, but also would lead to much longer simulation times on a serial processor for the kinetic approach over CFD. However, in LB one employs a minimal discrete lattice representation in ξ-space so that in the Chapman-Enskog limit one recovers the MHD equations (1) and (2).

In $D = 3$ spatial dimensions, one may show that with $Q = 27$ streaming velocities on a cubic lattice (*i.e.* the particles have discrete velocities $\mathbf{e}_\alpha$, $\alpha = 1, \cdots, Q$) up to fourth rank tensors made up of products of $\mathbf{e}_\alpha$ are isotropic. In turn, moments of the local particle distributions are isotropic up to 4th order. This is sufficient symmetry to recover isotropic fluidic behavior in the scaling limit characterized by parabolic (and nonlinear) equations of motion.[1]

The LB-MHD representation that recovers the MHD equations in the long-wavelength and long-time limit is a generalization of the 2D work of Dellar [2]

$$f_\alpha(\mathbf{x} + \mathbf{e}_\alpha, t+1) = f_\alpha(\mathbf{x}, t) - \frac{1}{\tau_u}\left[f_\alpha(\mathbf{x}, t) - f_\alpha^{eq}(\rho, \mathbf{u}, \mathbf{B})\right]$$

$$\mathbf{g}_\beta(\mathbf{x} + \mathbf{e}_\beta, t+1) = \mathbf{g}_\beta(\mathbf{x}, t) - \frac{1}{\tau_B}\left[\mathbf{g}_\beta(\mathbf{x}, t) - \mathbf{g}_\beta^{eq}(\mathbf{u}, \mathbf{B})\right], \tag{3}$$

where $\alpha = 1, \cdots, Q$ and $\beta = 1, \cdots, Q'$ with $Q' \leq Q$ since there will be less moment constraints to be satisfied by $\mathbf{g}_\beta$. $f_\alpha(\mathbf{x}, t)$ is the (scalar) velocity distribution function, and $\mathbf{g}_\beta(\mathbf{x}, t)$ is the vector magnetic distribution whose

---

[1] This model is known as the *D3Q27 lattice stencil* in the literature. The discrete streaming velocities for the particles are: 1 speed-0 (rest) particle, 6 speed-1 particles [permutations of $(0, 0, \pm 1)$], 12 speed-$\sqrt{2}$ particles [permutations of $(0, \pm 1, \pm 1)$] , and 8 speed-$\sqrt{3}$ particles [permutations of $(\pm 1, \pm 1, \pm 1)$].

lowest order moments satisfy

$$\sum_{\alpha=1}^{Q} f_\alpha = \rho, \quad \sum_{\alpha=1}^{Q} f_\alpha \mathbf{e}_\alpha = \rho \mathbf{u}, \quad \sum_{\beta=1}^{Q'} \mathbf{g}_\beta = \mathbf{B}_\beta. \tag{4}$$

The relaxation rates τ_u and τ_B determine the (macroscopic) viscosity and resistivity transport coefficients

$$\nu = c_s^2 \left(\tau_u - \frac{1}{2}\right) \qquad \eta = c_s^2 \left(\tau_B - \frac{1}{2}\right), \tag{5}$$

while f_α^{eq} and $\mathbf{g}_\beta^{eq}$ are the relaxed equilibrium distribution functions to which f_α and $\mathbf{g}_\beta$ are driven by the collisions, respectively. One is forced into a vector distribution representation for the magnetic field because of the antisymmetric magnetic stress tensor

$$\Lambda_{ij} = u_i B_j - u_j B_i \tag{6}$$

that generates (1b) as opposed to the symmetric momentum stress tensor

$$\Pi_{ij} = \left(\frac{\rho}{3} + \frac{1}{2}\mathbf{B}^2\right)\delta_{ij} + \rho u_i u_j - B_i B_j. \tag{7}$$

that generates (1a). These symmetry differences are preserved by defining the higher order moments as the second moment of f_α but the first moment of $\mathbf{g}_\beta$

$$\Pi_{ij} = \sum_{\alpha=1}^{Q} f_\alpha e_{\alpha i} e_{\alpha j} = \Pi_{ji}, \quad \Lambda_{ij} = \sum_{\beta=1}^{Q'} g_{\beta i} e_{\beta j} = -\Lambda_{ji}. \tag{8}$$

It can be shown that an appropriate set of equilibrium distributions that will lead to the MHD equations (1) and (2) under Chapman-Enskog perturbative expansion asymptotics are given by $Q = 27$ streaming velocities for f_α but fewer $Q' = 15$ streaming velocities[2] for $\mathbf{g}_\beta$

$$\begin{aligned} f_\alpha^{eq}[\rho, \mathbf{u}, \mathbf{B}] &= \rho w_\alpha \left[1 + 3\mathbf{e}_\alpha \cdot \mathbf{u} + \frac{9}{2}(\mathbf{e}_\alpha \cdot \mathbf{u})^2 - \frac{3}{2}\mathbf{u}^2\right] \\ &\quad + \frac{9}{2} w_\alpha \left[\frac{1}{2}\mathbf{B}^2 \mathbf{e}_\alpha^2 - (\mathbf{e}_\alpha \cdot \mathbf{B})^2 - \frac{1}{6}\mathbf{B}^2\right], \\ g_{\beta i}^{eq}[\mathbf{u}, \mathbf{B}] &= w'_\beta \left[B_i + 3e_{\beta j}(u_j B_i - u_i B_j)\right], \end{aligned} \tag{9}$$

where the normalized lattice weight factors (with $\sum_{\alpha=1}^{Q} w_\alpha = 1$, $\sum_{\beta=1}^{Q'} w'_\beta = 1$) for each speed w_α, w'_β are

$$\begin{aligned} &w_\alpha^{[0]} = \frac{8}{27}, \quad w_\alpha^{[1]} = \frac{2}{27}, \quad w_\alpha^{[\sqrt{2}]} = \frac{1}{54}, \quad w_\alpha^{[\sqrt{3}]} = \frac{1}{216}, \\ &{w'}_\beta^{[0]} = \frac{2}{9}, \quad {w'}_\beta^{[1]} = \frac{1}{9}, \quad {w'}_\beta^{[\sqrt{3}]} = \frac{1}{72}. \end{aligned} \tag{10}$$

where the superscript $[\bullet]$ means all permutations of directions for which the αth lattice vector has length $\bullet$.

II. PARALLEL LB-MHD ALGROITHM

There are two basic steps in the LB-MHD algorithm (3):

1. At each lattice point x there is local collisional relaxation ($\alpha = 1, \cdots, Q$)

$$\begin{aligned} f_\alpha(\mathbf{x}, t) - \frac{1}{\tau_u}\left[f_\alpha(\mathbf{x}, t) - f_\alpha^{eq}(\rho, \mathbf{u}, \mathbf{B})\right] &\to f'_\alpha(\mathbf{x}, t), \\ \mathbf{g}_\beta(\mathbf{x}, t) - \frac{1}{\tau_B}\left[\mathbf{g}_\beta(\mathbf{x}, t) - \mathbf{g}_\beta^{eq}(\mathbf{u}, \mathbf{B})\right] &\to \mathbf{g}'_\beta(\mathbf{x}, t), \end{aligned} \tag{11}$$

   with the fields $\mathbf{u}, \mathbf{B}$ being determined from the local moments (4).

2. Streaming of the post-collision distribution functions to the nearby lattice sites connected by the lattice vector $\mathbf{e}_\alpha$

$$\begin{aligned} f'_\alpha(\mathbf{x}, t) &\to f_\alpha(\mathbf{x} + \mathbf{e}_\alpha, t+1), \quad \alpha = 1, \cdots, Q \\ \mathbf{g}'_\beta(\mathbf{x}, t) &\to \mathbf{g}_\beta(\mathbf{x} + \mathbf{e}_\beta, t+1), \quad \beta = 1, \cdots, Q'. \end{aligned} \tag{12}$$

The collisional relaxation is relatively computationally intense compared to streaming–but only requires data that is local to that grid point. The streaming is a set of shift operations–and it is this step that requires message passing interface (MPI) between processing elements as one streams boundary points in the domain decomposition of the $D = 3$ space. A key optimization is the partial combination of the local of the local collisional relaxation with the streaming. Either the newly calculated post-collision distribution functions are streamed immediately to their new spatial grid as soon as they are calculated, or the data can be gathered from adjacent cells to determine the updated value for the current cell. While this makes more complex the memory access pattern for the collisional step, it significantly reduced the amount of data that needs to be transferred at each time step. This results in a computational speed-up of 20-30%.

A. Serial performance of LB-MHD: comparable performance to CFD codes

LB methods are explicit, Lagrangian finite-hyperbolicity representations of fluid equations [1]. While they are second-order accurate in space and time, it is empirically observed that in many LB simulations the accuracy of the scheme supercedes those from second order finite difference schemes. This is particularly the case for turbulence simulations, where it is typically

[2] This is known as the *D3Q15 lattice stencil* in the literature, employing discrete streaming velocities with speeds $0, 1$ and $\sqrt{3}$. That is, the particle streaming velocities are: 1 speed-0 (rest) particle, 6 speed-1 particles [permutations of $(0, 0, \pm 1)$], and 8 speed-$\sqrt{3}$ particles [permutations of $(\pm 1, \pm 1, \pm 1)$].

found that LB produces results of quasi-spectral accuracy, i.e., asymptotically exponential accuracy. It is thought that this occurs specifically for LB simulations because in the 2-step collide-stream algorithm exact mesoscopic conservation laws are preserved to machine accuracy. As a result, it seems that the prefactor in front of the quadratic decay of the numerical error with grid resolution is extremely small [1]. A key feature of LB methods is that there are no Poisson-like diffusion operators appearing in the formulation. The macroscopic ∇^2-diffusion operators are recovered implicitly from adiabatic relaxation of the stress tensors to local equilibrium (finite-hyperbolicty). Thus the very restrictive Courant-Friedrichs-Lewy (CFL) condition for explicit CFD schemes requires $\nu\Delta t < \Delta x^2$—and hence very small time steps. On the other hand, in LB the CFL constraint is that for simple advection: $c\Delta t < \Delta x$. Thus LB schemes are a special kinetic scheme whose efficiency and performance on a serial computer is on the order of CFD codes. This is somewhat surprising for general kinetic schemes whose serial performance is orders of magnitude worse than CFD schemes.

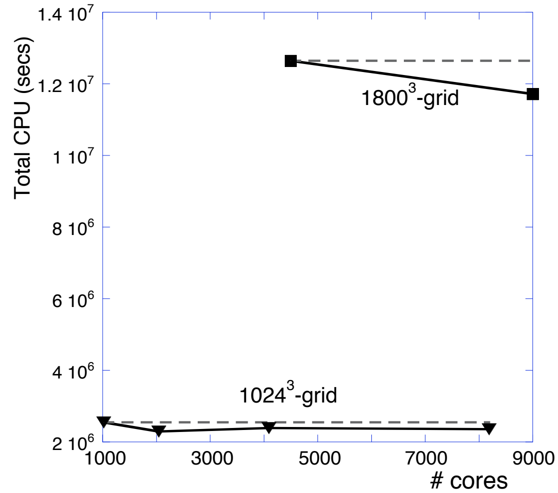

FIG. 1: Strong scaling results for the LB-MHD algorithm for two runs on the SGi-Altix 4700 at AFRL: (a) 1024^3-grid and (b) 1800^3-grid. The total CPU is plotted against the number of cores. The dashed curves are perfect strong scaling: for fixed grids, the wallclock time should be halved as the number of cores used doubles.

B. Parallel performance of LB-MHD

We have excellent strong scaling results for the LB-MHD code, run on the SGI-Altix Hawk. In Fig. 1 we show two runs: (a) a run on a spatial grid of 1024^3 , with the number of cores increasing from 1024 to 8192, and (b) a run on a spatial grid of 1800^3 at 4500 and 9000 cores. The total CPU time = wallclock time × no. of cores, and the dashed curves represent "perfect" scaling: doubling the number of cores halves the wallclock time and so gives constant total CPU. It is interesting to see that the 1800^3-grid run shows superlinear strong scaling: this possibly can be attributed to very efficient use of cache memory.

III. FREELY DECAYING MHD TURBULENCE

We consider the free decay of MHD turbulence for initial conditions arising from a Taylor-Green velocity field imbedded in an Orszag-Tang magnetic field (generalized to 3D):

$$\begin{aligned}\mathbf{u}\left(\mathbf{x},t=0\right) &= U_0\left(\sin x\cos y\cos z, -\cos x\sin y\cos z, 0\right),\\ \mathbf{B}\left(\mathbf{x},t=0\right) &= B_0\left(-2\sin 2y+\sin z, 2\sin x+\sin z, \sin x+\sin y\right).\end{aligned} \tag{13}$$

The initial isosurfaces of vorticity $\omega = \nabla\times\mathbf{u}$ and current $\mathbf{J} = \nabla\times\mathbf{B}$ are shown in Fig. 2 below. Initially the magnetic helicity and cross helicity are both zero

$$\begin{aligned}0 &= \int d^3x\ \mathbf{A}\left(\mathbf{x},0\right)\cdot\mathbf{B}\left(\mathbf{x},0\right),\\ 0 &= \int d^3x\ \mathbf{u}\left(\mathbf{x},0\right)\cdot\mathbf{B}\left(\mathbf{x},0\right),\end{aligned} \tag{14}$$

where $\mathbf{A}$ is the vector potential, $\mathbf{B} = \nabla\times\mathbf{A}$. Now from Chapman-Enskog asymptotics, one can show that the trace of the first order magnetic stress tensor is proportional to the divergence of the magnetic field. Since the magnetic stress tensor [see (6) and (7)] is antisymmetric

$$0 = \mathrm{Tr}\,\Lambda^{(1)} = \sum_{\beta,i} e_{\beta i}\left[g_{\beta i} - g_{\beta i}^{eq}\right] = -\frac{\tau_B}{3}\nabla\cdot\mathbf{B}. \tag{15}$$

This is verified in our LB simulations in which we explicitly calculate the trace of the magnetic stress tensor, and find numerically that $\mathrm{Tr}\,\Lambda^{(1)} = 0$ to machine accuracy. Thus LB-MHD automatically ensures the $\nabla\cdot\mathbf{B} = 0$ constraint is satistfied, without any need for divergence cleaning.

We now discuss one of our major runs on an 1800^3-spatial grid using all the 9000 cores on the AFRL SGI Altix Hawk. This run had Reynolds number $\mathrm{Re} = U_0L/\nu = 350$, magnetic Reynolds number $\mathrm{Rm} = U_0L/\eta = 1050$ and a magnetic Prandtl number $\mathrm{Pr} = \nu/\eta = 3$. In Fig. 3, one clearly sees the intensification of localized horizontal current sheets, the development of intense vertical patches of vorticity and current at later times with similar geometric structures, Moreover, unlike normal fluid turbulence, large scale structures in both the magnetic and velocity fields persist throughout the simulation.

The longitudinal and transverse correlations for $\mathbf{u}, \mathbf{B}, \omega, \mathbf{J}$ are defined by

$$\begin{aligned}C^u_{\mathrm{long}}(r,t) &= \left\langle u_x\left(x,y,z,t\right)u_x\left(x+r,y,z,t\right)\right\rangle,\\ C^u_{\mathrm{trans}}(r,t) &= \left\langle u_y\left(x,y,z,t\right)u_y\left(x+r,y,z,t\right)\right\rangle.\end{aligned} \tag{16}$$

with corresponding definitions for $\mathbf{B}, \omega, \mathbf{J}$. The time evolution of these correlations are shown in Fig. 4. The

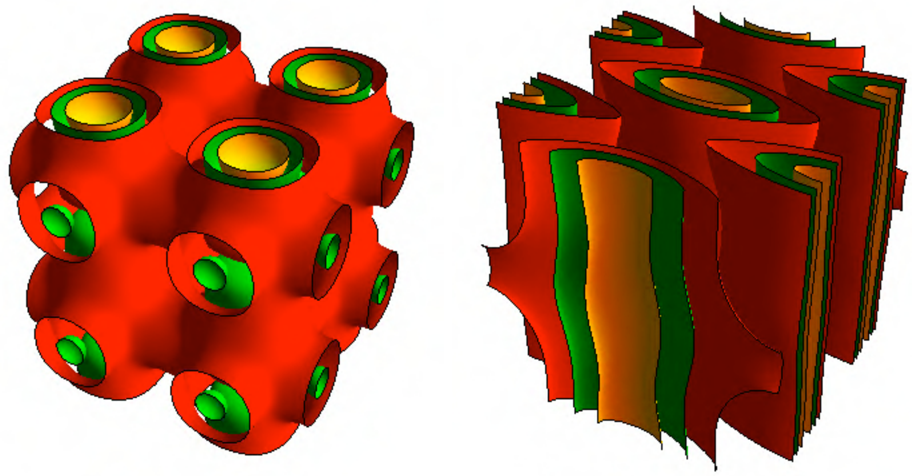

FIG. 2: The initial isosurfaces for the absolute value of vorticity (left) and current (right).

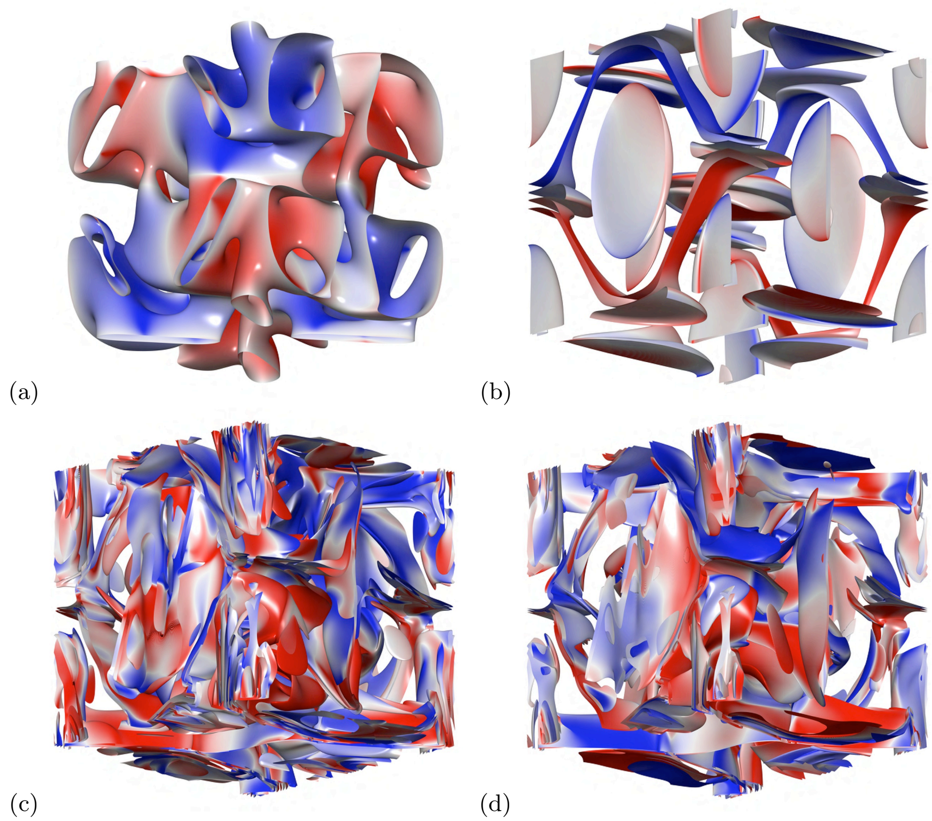

FIG. 3: (a) Isosurfaces of the vorticity $|\omega|$ at early time in the evolution, $t = 4K$ and (b) current isosurfaces $|\mathbf{J}|$ at $(t = 4K)$. Both large and small scale structures persist at $t = 24K$ – (c) vorticity isosurface, and (d) current isosurface. Color coding: RED when $\hat{\mathbf{u}} \cdot \hat{\omega} = 1 = \hat{\mathbf{B}} \cdot \hat{\mathbf{J}}$, BLUE when $\hat{\mathbf{u}} \cdot \hat{\omega} = -1 = \hat{\mathbf{B}} \cdot \hat{\mathbf{J}}$, and GREY when $\hat{\mathbf{u}} \cdot \hat{\omega} = 0 = \hat{\mathbf{B}} \cdot \hat{\mathbf{J}}$.

solid curves are for the longitudinal correlations and the dashed curves are for the transverse correlations. The time evolution of these correlations is given by color coding : green ($t = 4K$), blue ($t = 16K$) and red ($t = 28K$). The initial long range correlations in all but the longitudinal magnetic field correlations are rapidly destroyed by the turbulence. As expected, the vorticity and current correlations become very short range and for large times there is little distinction between the longitudinal and transverse correlations. Of some interest is the

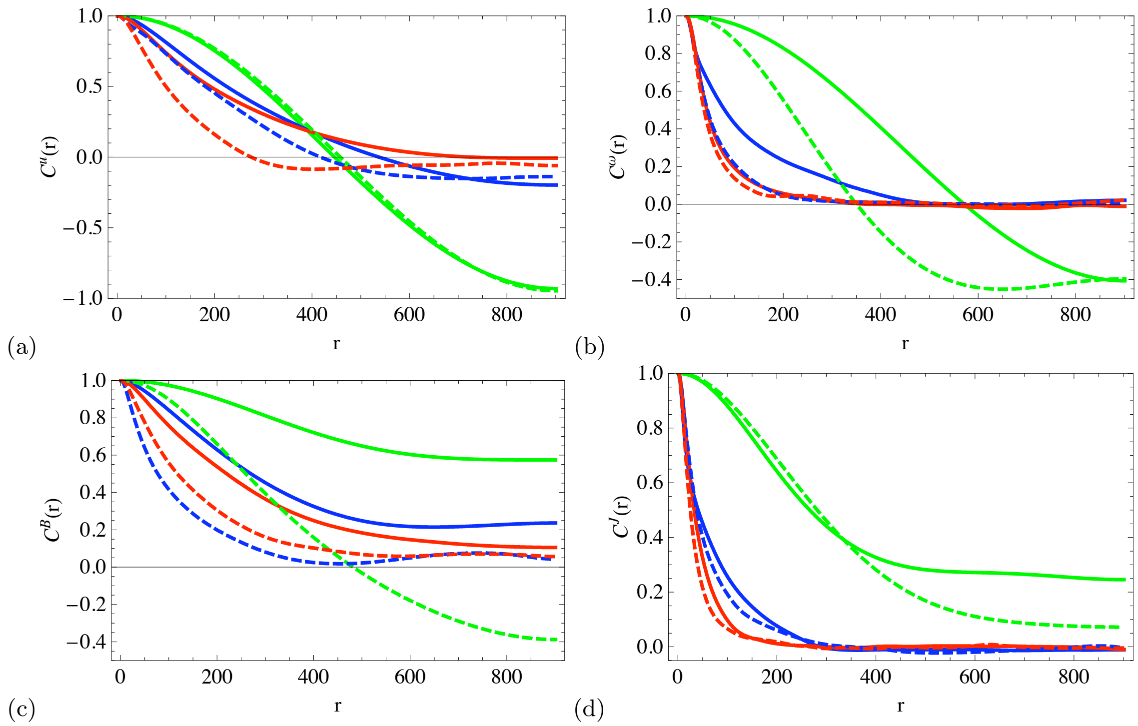

FIG. 4: The time evolution of the longitudinal and transverse correlation functions for (a) velocity, (b) vorticity, (c) magnetic, and (d) current fields. The longitudinal correlations (solid curves) and the transverse correlations (dashed curves) are plotted for $t = 4K$ (green), $t = 16K$ (blue) and $t = 28K$ (red).

comparison of the longitudinal and transverse magnetic correlations. We see that for all times the transverse magnetic correlations are always bounded by the longitudinal magnetic correlations for each separation r: $C^B_{\text{trans}}(r,t) < C^B_{\text{long}}(r,t)$. Moreover, the derivative of the longitudinal magnetic correlation becomes monotonic later in their evolution: . This is consistent with the correlation statistics of a random solenoidal vector field [4]. This indicates that the magnetic field is tending more and more towards a random (solenoidal) vector field. The solenoidal property of B has been preserved throughout the simulation to machine accuracy.

Finally, we consider the evolution of the probability distribution functions (pdf's) for u_z, ω_z, B_z, J_z in time. In Fig. 5 these are shown at times $t = 4K$ and $t = 28K$. In the frames $(a) - (d)$ at $t = 4K$ one sees the early stage development of the pdf's. By $t = 28K$, the velocity and magnetic field tend towards Gaussians–although the magnetic field has broader tails. The vorticity and current pdf's tend towards exponentials–indicative of intermittency in the turbulence.

IV. ACKNOWLEDGEMENTS

The authors were supported by grants from DoE, AFOSR and AFRL. The simulation results were obtained under a Capability Application Project on the Department of Defense Major Shared Resource Centers at the Air Force Research Laboratory.

[1] S. Succi, *The Lattice Boltzmann Equation for Fluid Dynamics and Beyond,* Clarendon Press, 2001 - and references therein.

[2] P. J. Dellar, Lattice kinetic schemes for magnetohydrodynamics, J. Comp. Phys. **179**, (2002) 95-126

[3] G. Vahala, B. Keating, M. Soe, J. Yepez, L. Vahala, J. Cater and S. Ziegeler, Comm. Comp. Physics, to appear, Sept. 2008

[4] S. Panchev, *Random Functions and Turbulence*, Pergamon Press, 1971.

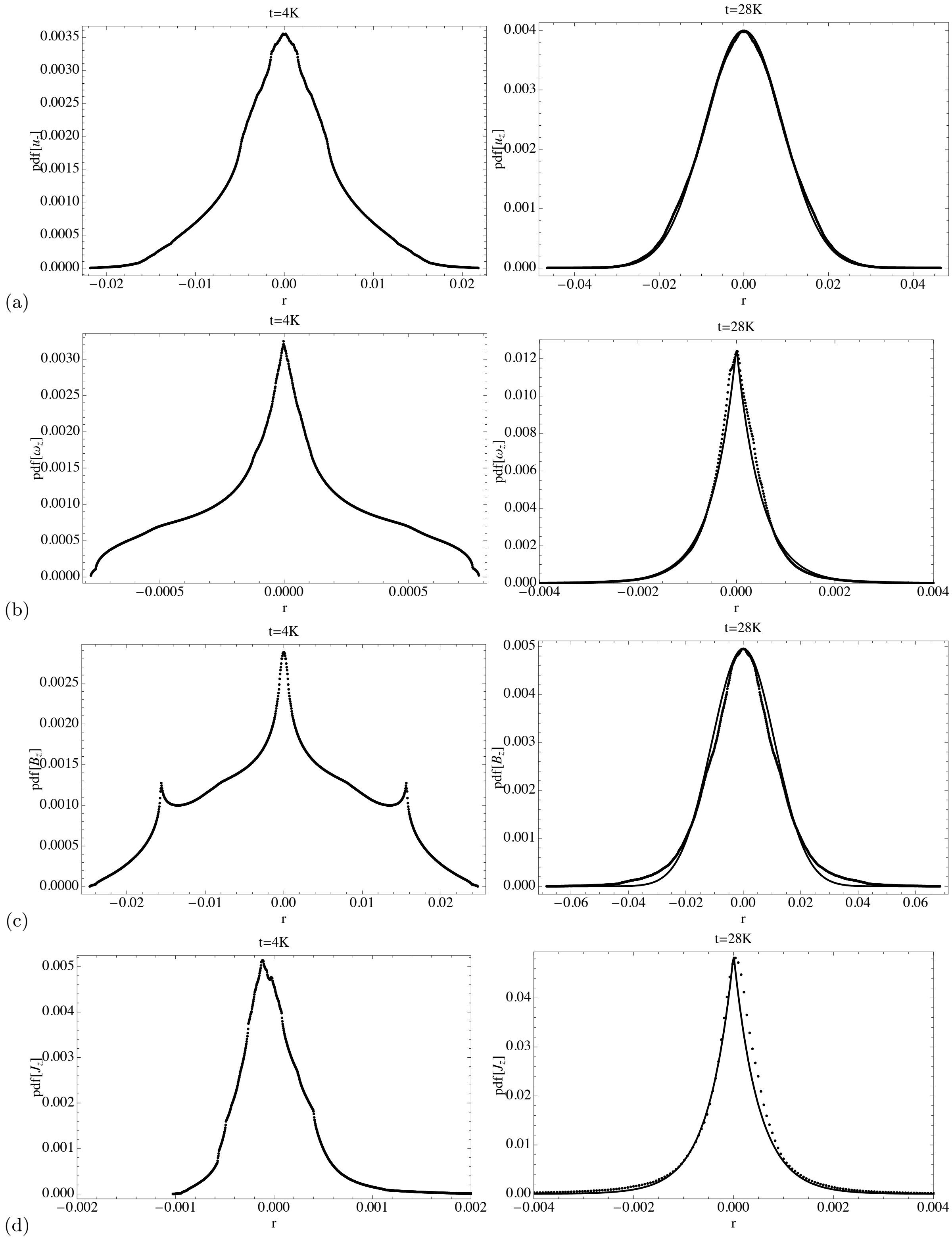

FIG. 5: Correlations versus separation distance pdf's. The pdf's at early times are non-normal, indicative of highly anisotropic flows; for example, the pdf's at $t = 4K$ are shown (left side). Numerical data (dots) and theoretical fit (solid curves) are compared at $t = 28K$ (ride side). At late times, the velocity and magnetic field pdf's approach Gaussians and the vorticity and current approach exponentials, a consequence of isotropic flow fields.